Scripta Materialia 227 (2023) 115297

Contents lists available at ScienceDirect

Scripta Materialia

journal homepage: www.journals.elsevier.com/scripta-materialia

The interfacial stability of single crystal superalloy affected by the phase structure of the Ni-Al coating

Jiao Wen [a,b], Jingyong Sun [a,b,*], Boxuan Du [a,b], Yu Chen [c], Xin Yan [c,*]

[a] School of Materials Science and Engineering, Beihang University, Beijing 100191, China
[b] Key Laboratory of High-Temperature Structural Materials &Coatings Technology (Ministry of Industry and Information Technology), Beijing 100191, China
[c] School of Mechanical Engineering and Automation, Beihang University, Beijing 100191, China

ARTICLE INFO

Keywords:
Ni-Al coating
Single crystal superalloy
Interfacial stability
Nudged elastic band calculation

ABSTRACT

Interfacial stability between the bond coating and single crystal superalloy substrate is crucial for their long-term performance at elevated temperatures. Herein, we designed coatings with various phase structures and used the typical single crystal superalloy René N5 as the substrate to investigate the intrinsic mechanism underpinning recrystallization using experiments combined with atomistic simulations. Experimentally, recrystallization occurred in the specimen with coatings of medium Al content (CA-25 specimen); in contrast, there was no secondary reaction zone in the CA-30 specimen with coatings of the highest Al content. From simulations, the nudged elastic band calculation demonstrated that a higher energy barrier (ΔE_0) was required for new grain nucleation in the substrate under β-NiAl grains, which existed in the CA-30 coating. Our findings provide a fundamental understanding of interfacial stability and benefit the design of bond coatings for superalloys.

Ni-Al alloys have attracted considerable research and development efforts because of their excellent high-temperature oxidation resistance [1–4]. Based on its low-density and superior mechanical properties, the Ni-Al coating is a potential candidate for the bond coating of superalloys [5,6]. However, interdiffusion between the metallic coatings and the superalloy substrate is inevitable due to the element concentration gradient, especially at elevated service temperatures. Generally, the inwards diffusion of Al destroys the initial γ/γ′ structure of the superalloy substrate and results in the precipitation of topologically close-packed (TCP) phases [4,7,8]. Moreover, recrystallization occurs in a single crystal (SC) superalloy, and a secondary reaction zone (SRZ) forms during service, leading to a higher density of TCP phases and substrate instability [9]. The formation of the SRZ introduces high-angle boundaries for rapid diffusion, which accelerate the creep property deterioration of the SC superalloy [10–12]. Therefore, understanding the formation of the SRZ and restraining its growth has been an essential topic for the application of Ni-Al coatings.

Typically, the SRZ-type instability is predominantly determined by the inwards diffusion of the Al element from the bond coating to the superalloy substrate [9,13]. Even so, the structural features of the substrate and coatings, such as crystal orientation and lattice parameters, cannot be ignored. Pioneer investigations have indicated that the phase forming procedure is modified by the crystallographic orientation of the SC superalloy substrate. For example, Hong et al. reported the preferential formation of the SRZ along the (011) direction [10], while Wang et al. observed a thicker SRZ layer in the (011) crystal orientation specimen than in the (001) specimen [2]. According to these studies, recrystallization is associated with the lowest interfacial energy [10,14]. Nonetheless, the coating phase structure, which modifies the interfacial energy, has rarely been considered.

Basically, recrystallization takes place when the driving force is higher than the critical value [15]. Microstructural development and deformation-driven recrystallization have been carried out by cellular automaton and Monte Carlo [16,17]. In addition, some theoretical work uses Eshelby inclusion theory, which is advanced in relating microstructure to the macro properties of the materials [18,19], to describe the recrystallization [20]. However, there are difficulties in describing the recrystallization occurrences with the impact of coatings using theoretical approaches. Specifically, it is challenging to clarify the influence of the crystal structure and lattice parameter difference at the interface from the atomic point of view. Molecular dynamics (MD) simulations enable the investigation of atom movement at grain boundaries and interfaces [21–23]. In principle, using MD simulations, the nudged elastic band (NEB) method quantifies the activation barriers

* Corresponding authors.
E-mail addresses: sunjingyong@buaa.edu.cn (J. Sun), yan_xin@buaa.edu.cn (X. Yan).

https://doi.org/10.1016/j.scriptamat.2023.115297
Received 27 June 2022; Received in revised form 7 November 2022; Accepted 5 January 2023

for given reactions and determines the minimum energy pathway. Thus, the NEB calculation would provide an evaluation of the energy barrier of the structure before and after recrystallization [24–26]. Above all, a combination of experimental studies and NEB calculations could reveal the role of the coating structure in SRZ formation and substrate recrystallization.

In this work, we designed and deposited Ni-Al coatings with different phase structures on a SC superalloy substrate; then, the specimens were heat-treated at an elevated temperature (1100 °C). The substrate stability after annealing for short and long times was analysed by transmission electron microscopy (TEM) and electron backscattered diffraction (EBSD). Subsequently, based on the experimental results, we performed NEB calculations on superalloy models with Ni-Al coatings of various phase structures to examine the role of the coating structure in substrate recrystallization. Finally, the activation energy obtained by NEB calculation was coupled with orientation imaging microscopy (OIM) maps to investigate the substrate stability. This work focuses on the microstructure stability of a superalloy, aiming to provide a guideline for Ni-Al coating design and propose an investigation strategy for the recrystallization of the SC superalloy.

The second-generation Ni-based SC superalloy René N5 was used as a substrate. Disk-shaped specimens with dimensions of Φ15 × 2 mm^2 along the (001) plane were prepared (more details of the superalloy are available in the Supplementary Materials). Ni-Al coatings with various element ratios were deposited on the substrate by electron beam-physical vapour deposition (EB-PVD) following our previous work [27]. Then the specimens with the Ni-Al coating were annealed in a vacuum at 1100 °C for specific hours to investigate the interfacial properties. The cross-sectional micromorphologies of the specimens were analysed by scanning electron microscopy (SEM, Gemini SEM 300, Zeiss, Oberkochen, Germany) at 10 kV. The microstructures were investigated by TEM (FEI Tecnai G2 F20) at 200 kV. The foil for TEM was cut and lifted out by a focused ion beam (FIB). The element analyses were conducted by an energy dispersive spectrometer (EDS, Bruker). The orientation maps of the coating and substrate were characterized by a field emission SEM (Apollo 300) equipped with an EBSD analyser.

The NEB calculation was performed using a large-scale atomic/molecular massively parallel simulator (LAMMPS) [28]. The simulation model composed of a polycrystalline Ni_3Al/NiAl coating and SC superalloy is shown in Fig. 1 (see Supplementary Materials for more details of the model). To represent the nucleation embryo of a new grain, a hemisphere atom cluster with a radius of 12 Å in the substrate was selected and rotated around the *z*-axis by 75°. The coating/substrate model with the cluster before and after rotation served as the initial and final structures for NEB calculation. The EAM potential developed by Mishin et al. was used to describe the interatomic interactions between Ni and Al atoms [29]. Periodic boundary conditions were applied along the *x*- and *y*-directions. We remark that our NEB models were simplified, in which elements with low fractions in the real material, such as Re and W, were not considered [30]. The simulation models were visualized by OVITO [31].

The Ni-Al coatings with distinct phase structures, predicted by the Ni-Al phase diagram (calculated by Thermo-Calc [32] and illustrated in Supplementary Materials SFig. 2), were realized by various element ratios. Specifically, the Ni-Al alloy with 20 at.% Al is composed of γ (Ni) and γ′ (Ni_3Al) phases, the Ni-Al alloy with 25 at.% Al consists of the γ′ (Ni_3Al) phase, and the Ni-Al alloy with 30 at.% Al contains γ′ (Ni_3Al) and β (NiAl) phases (for atomic structures of the γ, γ′, and β phases, please refer to the Supplementary Materials). Generally, the Ni/Al ratio of the coating deviates from that of the ingot during deposition by EB-PVD. Hence, ingots with a larger Al proportion than expected were prepared (shown in Table 1). Elements of the as-deposited coatings are shown in Table 1, whose Ni/Al ratios were near those predicted and positioned inside the expected phase diagram regions. The phase structures of the coatings were confirmed by XRD patterns and SEM images (see Supplementary Materials). The specimens were named after the expected Al ratio of the Ni-Al coating: CA-20 has a two-phase (γ+γ′) coating, CA-25 has a single-phase (γ′) coating, and CA-30 has a two-phase (γ′+β) coating.

To gain insight into the character of the substrate after annealing, the microstructures after a short time (20 h) were analysed by SEM and

Table 1
Chemical compositions of the ingots and the deposited coatings (CA) (in at.%).

	ingots		coatings	
	Ni	Al	Ni	Al
CA-20	74.13	25.87	78.98	21.02
CA-25	70.00	30.00	73.37	26.63
CA-30	65.00	35.00	68.28	31.72

The specimens were named after the expected Al atomic proportion of the coatings.

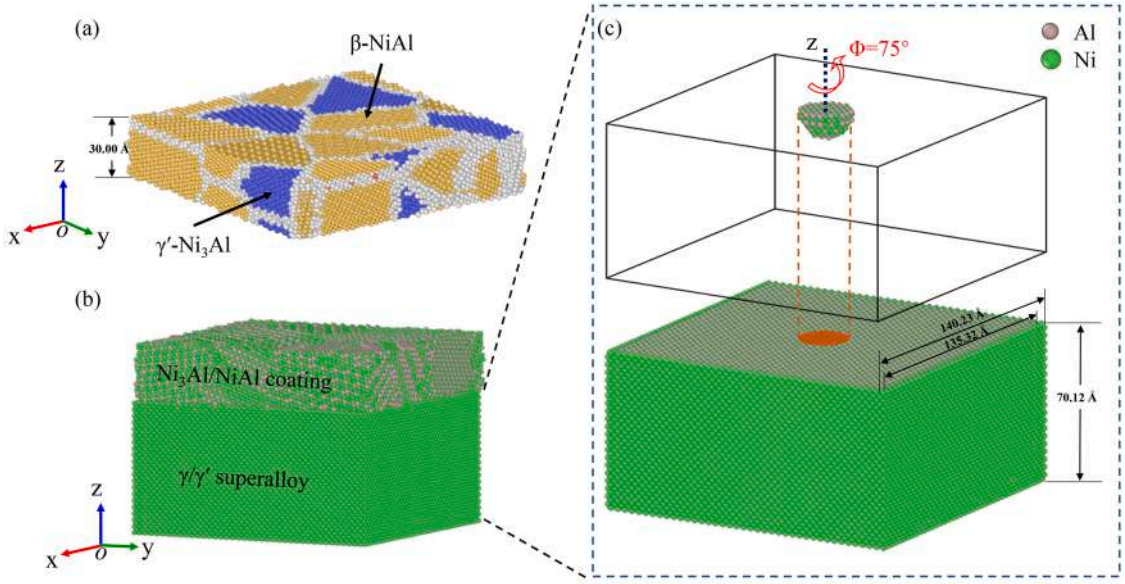

Fig. 1. Atomic model for NEB calculation. (a) polycrystalline coating with β-NiAl (yellow) and γ′-Ni_3Al (blue) phases; (b) the NEB model of polycrystalline Ni-Al coating/superalloy substrate; (c) the rotation cluster in γ′ phase for NEB calculation.

TEM. The cross-sectional morphology of the CA-20 specimen is shown in Fig. 2a. Clearly, interdiffusion behaviour of the elements occurred because of the Al and Ni content difference between the deposited coating and the superalloy substrate. Furthermore, the TEM image of the rectangular region in Fig. 2a is presented in Fig. 2b, and the selected area electron diffraction (SAED) pattern revealed the γ′ phase (region I) and a small amount of γ phase (region II). There were no TCP phases precipitated from the SC superalloy substrate, probably because of the residue of γ phases.

For the CA-25 specimen, which had a higher percentage of Al element in the coating, the transformation from γ to γ′ would be accelerated in principle. More Ni-rich phases were observed (bright contrast) in the coating near the substrate as the Al element diffused into the substrate (Fig. 2c). Meanwhile, needle-shaped TCP phases precipitated in the substrate due to the release of the refractory elements, and the EDS patterns in SFig. 7 showed enrichment of Re, W, and Co elements. The SAED pattern taken from region III (dark contrast) reflected the μ phase structure for the TCP phase [33]. The destroyed region in the substrate of the CA-25 specimen consisted of the γ′ phase, as shown in SFig. 7 (region V). In addition, there were grain boundaries in the foil for TEM, and a twin structure of the γ′ phase was observed in the substrate.

In regard to the CA-30 specimen, which had the highest Al element ratio in the coating, the inwards diffusion of the Al element also resulted in a Ni-rich area in the coating near the substrate (the cross-sectional morphology of CA-30 is shown in Fig. 2e). At the same time, the volume fraction of precipitate particles in the substrate was more significant (more details are available from the TEM image (Fig. 2f)). Two kinds of TCP phases precipitated in the CA-30 specimen, and the TEM images reflected platelet (region IV in Fig. 2f) and needle-shaped (region VI in SFig. 8a) TCP phases. The SAED pattern of the needled-shaped TCP phase presented the same parameters as the TCP phase in the CA-25 specimen, which was revealed to be the μ phase. The SAED pattern of the platelet TCP phase showed features of the Laves phase (region VII). Furthermore, the platelet TCP phase exhibited a coherent relationship with the γ′ phase substrate, as shown in SFig. 8b. Consequently, we demonstrated that the phase structure of the substrate was affected by the coating element ratio: inwards diffusion of more Al depleted the γ phases in the substrate and promoted the precipitation of the TCP phases.

A further investigation was conducted to identify the phase stability of the substrate with different Ni-Al coatings at 1100 °C. The OIM maps of the Ni-Al coating/superalloy substrate after long-term heat treatment are illustrated in Fig. 3. The Ni-Al coatings deposited by EB-PVD exhibited polycrystalline structures with average grain sizes of 10~15 μm. After a long annealing time, the phase structure of the substrate was drastically influenced by the inwards diffusion of Al element from the coatings.

The inverse pole figure (IPF) map of the CA-20 specimen (Fig. 3a) shows that after annealing for 100 h, the substrate remained a single crystal along the (001) direction, and a substrate diffusion zone (SDZ) was formed. In contrast, recrystallization occurred and an SRZ was formed in the CA-25 specimen after annealing for the same period (Fig. 3c). The network of the grain boundaries for CA-25 is also shown in Fig. 3d, and high-angle boundaries were introduced into the substrate

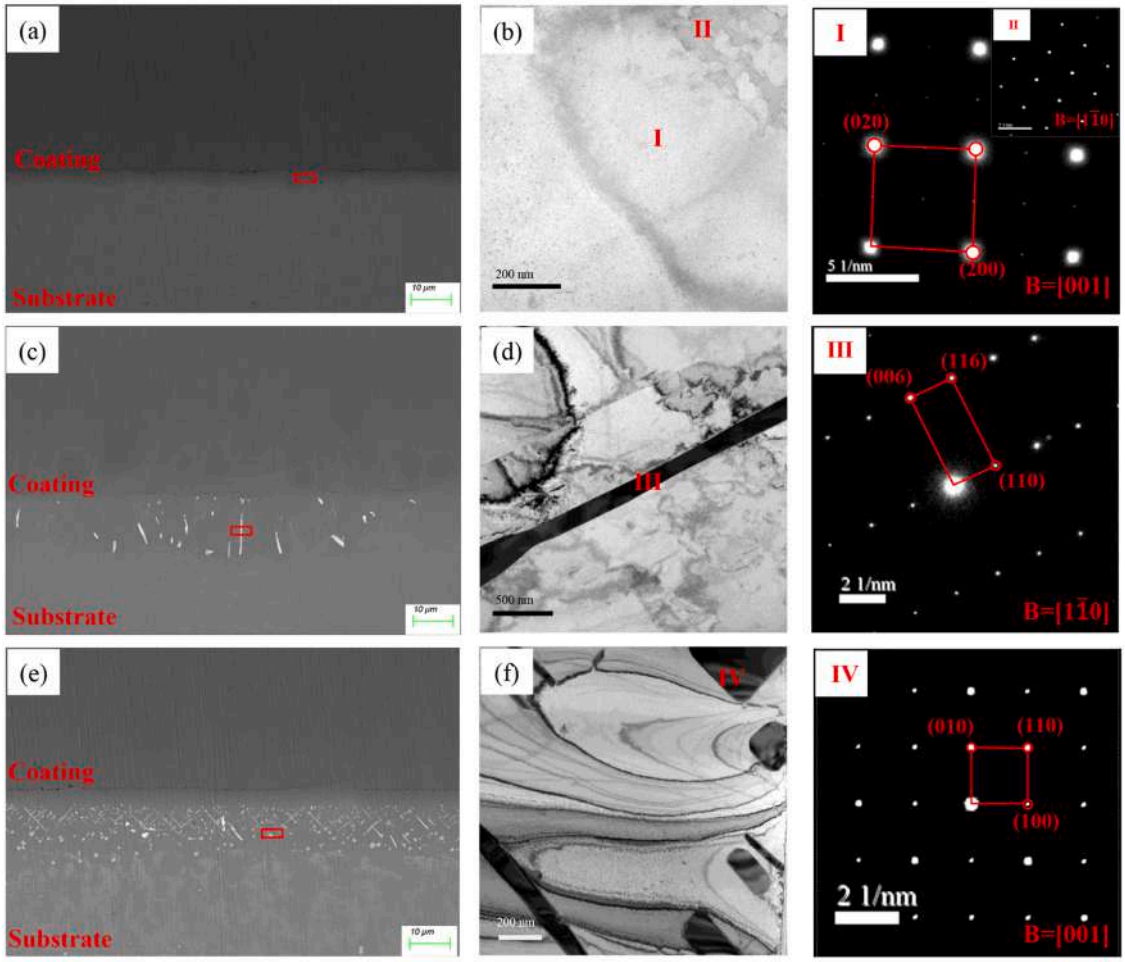

Fig. 2. Microstructural details of the specimens after annealing for 20 h at 1100 °C. (a) SEM image of CA-20 specimen; (b) bright-field TEM image and SAED patterns for the phase identification in (a); (c)(d) SEM and TEM images for CA-25 specimen; (e)(f) SEM and TEM images for CA-30 specimen.

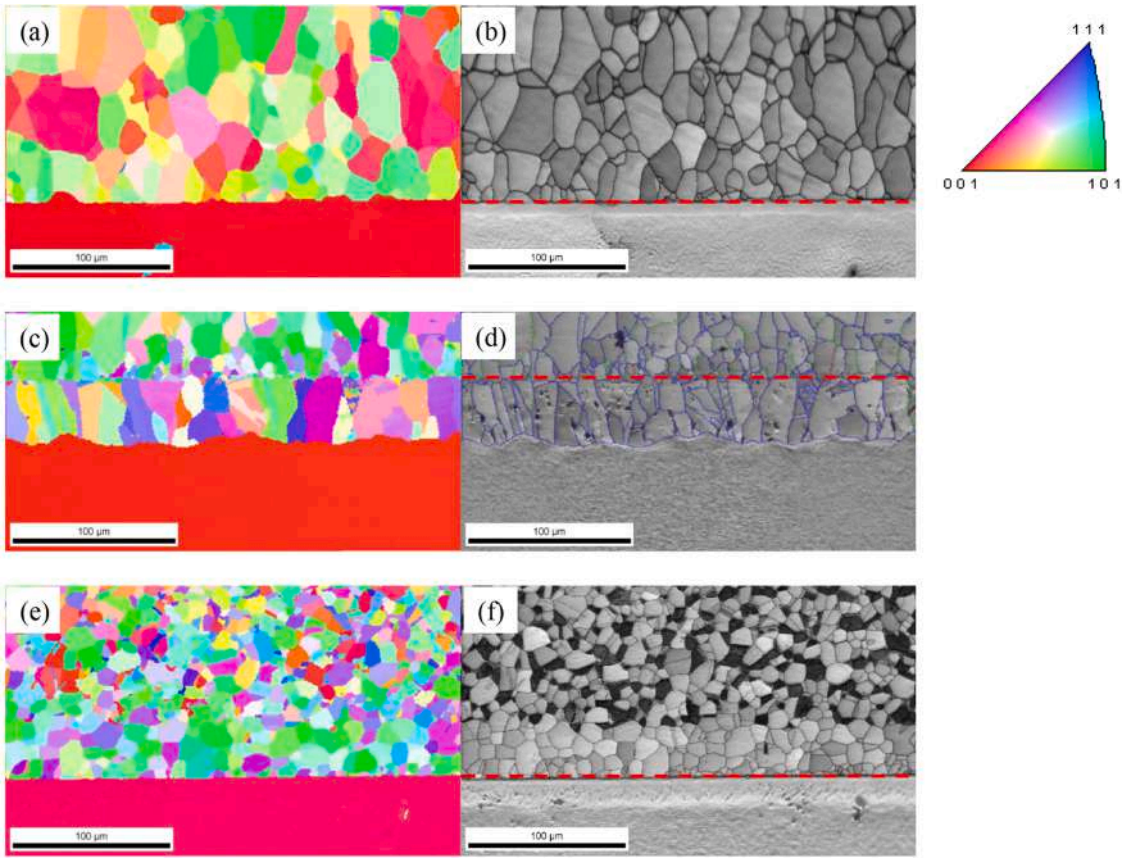

Fig. 3. OIM maps of the Ni-Al coating/superalloy substrate after annealing for 100 h at 1100 °C. IPF maps and Image quality (IQ) maps for (a)&(b) CA-20, (c)&(d) CA-25, and (e)&(f) CA-30 (the red dot lines represent the initial boundaries between the bond coating and substrate).

during annealing (the blue line represents boundaries with angles larger than 15°). However, for CA-30, although the ratio of Al elements was further increased and more TCP phases precipitated, the substrate maintained a single crystal, and an SDZ also formed in the substrate (Fig. 3e).

The emergence of polycrystals in Fig. 3c is usually defined as diffusion-induced recrystallization (DIR) [34], which describes the formation of new grains due to atom diffusion. According to previous investigations, the occurrence of DIR is determined by the element interdiffusion between the coating and the substrate, which promotes the generation of an SRZ [10,34]. As expected, the massive inwards diffusion of Al caused the substrate structure to transform, and more TCP

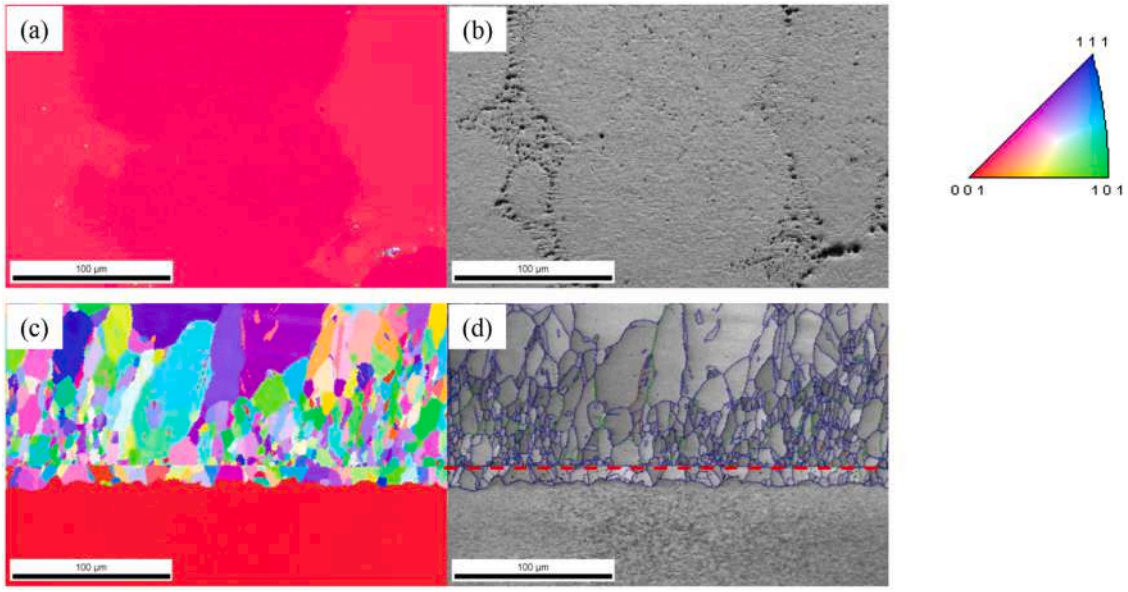

Fig. 4. OIM maps for the René N5 substrate after annealing for 100 h at 1100 °C. (a) IPF map; (b) IQ map; OIM maps for CA-25 after annealing for 5 h at 1100 °C; (c) IPF map; (d) IQ map with grain boundaries (the red dot lines represent the initial boundaries between the bond coating and substrate).

phases precipitated because of the γ phase diminution in the CA-30 specimen. However, the substrate of the CA-30 specimen retained a single-crystal orientation even after a long annealing time. In comparison, an SRZ formed in the CA-25 specimen, which had a coating with a medium Al element ratio but a single γ′ phase. To eliminate the influence of substrate structural instability, the René N5 substrate without coatings was examined as well. The SC superalloy was annealed in a vacuum at 1100 °C for a long time (100 h), and EBSD analysis was performed. As shown in Fig. 4a&b, the SC superalloy maintained its initial (001) orientation, and there was no recrystallization without the impact from coatings. Hence, the recrystallization that occurs in the SC superalloy at elevated temperatures is induced by the Ni-Al coatings.

Theory based on free energy minimization has proposed that lowering the interface energy in CA-25 may lead to an easier nucleation process. For the CA-25 specimen, the coating with a single γ′ phase has lattice parameters similar to those of the substrate. By comparison, for the double phases in CA-30, the lattice parameters of the β phases are significantly different from those of the substrate, and more energy might be required for new phase nucleation in the substrate. A more detailed examination was carried out on the CA-25 specimen, and the IPF map after annealing for 5 h is shown in Fig. 4c. An SRZ formed after annealing for a short time; thus, recrystallization may occur at the very beginning. Therefore, it is more likely that the polycrystalline coating phase structure, rather than inwards element diffusion, results in the substrate instability in the CA-25 specimen. Moreover, it has also been confirmed that the new grain nucleates epitaxially with grains in the coated layer to gain the lowest interfacial energy [10]. Furthermore, the high-angle boundaries observed in CA-25 provided a rapid diffusion path and accelerated the growth of the SRZ. Therefore, the SRZ in the CA-25 specimen was much thicker than the SDZ in the CA-20 and CA-30 specimens after annealing for 100 h

To clarify the role of interfacial energy during recrystallization, NEB calculations were carried out on 30 models with different polycrystalline coatings. These polycrystalline coatings had the same grain size and distribution, but the crystal structure in Fig. 1a of each grain varied, and more structural information on the polycrystalline coatings is available in STable 2. As mentioned before, the cluster located at the top centre of the substrate rotated, and the models were classified by the grain type in the coating above the rotated cluster. In detail, CA-FCC represents the models whose grain 2 in coatings is γ′ phase (the grain marked by red region in Fig. 5a), and CA-BCC models have grain 2 that is β phase. Additionally, two substrate models were established, and the cluster was located in the centre of the γ′ phase and γ phase (Fig. 1b and SFig. 10a).

The NEB calculation determined the energy barrier (ΔE_0) for the cluster rotation, and the minimum energy path along the cluster rotation in the γ′ phase is plotted in Fig. 5b (minimum energy path for the cluster rotation in the γ phase is plotted in SFig. 10b). The curve showed a smooth transition procedure, and ΔE_0 was defined by the difference between the maximum value in the curve and the initial energy (we set the initial reference energy to 0 eV). The ΔE_0 values with different Ni/Al ratios of the coating are indicated in Fig. 5c (rotated cluster in the γ′ phases) and Fig. 5d (rotated cluster in the γ phases). Obviously, ΔE_0 of CA-BCC was larger than that of CA-FCC in both the γ′ and γ phases, which means that more energy is required for the cluster under a BCC grain to rotate. We note that the rotated cluster contains the same number of atoms in the CA-FCC and CA-BCC models. Meanwhile, the Ni/Al ratio showed no impact on the energy barrier, and ΔE_0 in this work was only influenced by the grain structure above the rotated cluster in the coating.

As mentioned above, the NEB calculation carries out potential energy landscape scanning and offers the minimum energy path for substrate recrystallization. The NEB calculation for the cluster rotation is

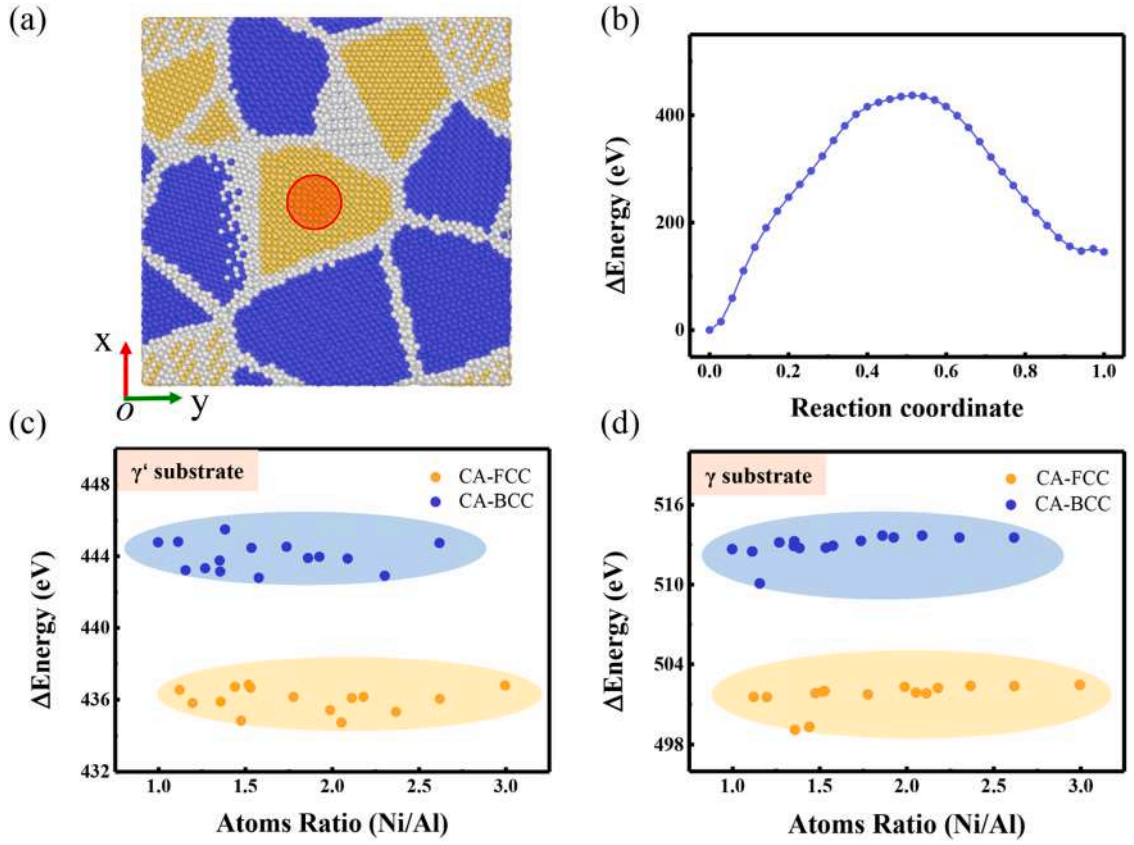

Fig. 5. NEB calculation for Ni-Al coating/superalloy substrate. (a) polycrystalline model of coating and the red area was above the cluster; (b) one of the typical minimum energy paths along with the cluster rotation of models (taking coating 1 in STable 2 as an example); energy barrier (ΔE_0) for the cluster rotation with cluster in (c) γ′ phase and (d) γ phase.

performed at zero temperature, ignoring the entropic contribution and assuming that the barrier on the potential energy surface is close to the barrier on the free energy surface [24]. Actually, the entropic is negligible under certain circumstances [35]. In addition, the impact of entropic to free energy might be close at the same temperature, as the difference between the initial and final states is similar amongst the coating/substrate models. Efforts on the energy barrier calculation considering the temperature effect are paid [36,37], and a more precise analysis might be necessary for further investigation.

The higher energy barrier for the cluster to rotate under the BCC grain demonstrated the formation of nucleation embryos, and further growth of the new grain was more difficult. Moreover, for the cluster in the γ phase, the absolute value of the energy barrier was higher under the same coating than in the γ′ phase, as shown in Fig. 5c and Fig. 5d. Concretely, the cluster rotation in the γ′ phase required ~445 eV under a β-NiAl grain and ~513 eV in the γ phase. Thus, recrystallization preferentially occurred in the γ′ phase rather than in the γ phase. Consequently, the NEB calculation showed that the energy barrier of the nucleation embryo formation was governed by lattice parameter mismatch and constituent of the cluster.

Inwards diffusion of Al from the bond coating to the SC superalloy substrate has long been recognized as the decisive factor for interfacial stability. Anomalously, recrystallization occurred in the CA-25 specimen with a coating of a medium Al element ratio; by comparison, the SC superalloy substrate of the CA-30 specimen, which had the highest Al content in the coating, maintained its original orientation. Thus, the coating phase structure may also play an essential role in interfacial stability. Indeed, the effect of the superalloy substrate orientation has been confirmed. From the perspective of interfacial energy, the coating structure and substrate orientation both follow the minimum energy required for recrystallization. The reduction in free energy (ΔE_{RX}) equation (Eq. (1)) proposed by Burgel et al. describes the factors for recrystallization as follows [14]:

$$\Delta E_{RX} = \Delta E_{mechanical} + \Delta E_{interface} + \Delta E_{chemical} \quad (1)$$

where $\Delta E_{mechanical}$ reflects the annihilation of dislocations and is not taken into consideration because of the same experimental conditions, $\Delta E_{interface}$ describes the influence of the grain boundaries and is related to the phase microstructures, and $\Delta E_{chemical}$ is determined by chemical compositions. It is notable that the CA-25 specimen consisted of the γ′ phase, which was the same as the substrate; in comparison, the β phase existed in the CA-30 coating, which was largely different from the substrate. In particular, the NEB calculation was carried out after energy minimization, and there was no element diffusion between the coating and substrate in the model. The energy barrier for recrystallization obtained by NEB calculation reflected the role of $\Delta E_{interface}$ between the Ni_3Al or NiAl grain in the coating and the substrate. Thus, the NEB results proved that with BCC grains in the Ni-Al coating, more energy was required for the substrate to recrystallize. The effect of the coating phase structure was further verified, as recrystallization occurred at the very early stage of annealing in the CA-25 specimen. Above all, we demonstrated that the interfacial stability of the SC superalloy René N5 was dominated not only by the inwards diffusion of Al but also by the phase structures of the Ni-Al coating.

In summary, we performed experimental studies and NEB calculations to investigate SC superalloy stability. Ni-Al coatings with three kinds of phase structures were deposited on the René N5 superalloy and annealed at 1100 °C. The substrate of the CA-30 specimen maintained the (001) orientation, while recrystallization occurred in the CA-25 specimen, and an SRZ was formed, although the former had the highest Al content in the coating. The impact of the coating phase structure was considered and examined by the interfacial energy barrier method. The NEB calculation with different coating phase structures showed a higher energy barrier for the substrate to recrystallize under a BCC grain. The CA-30 specimen, which contained β-NiAl grains in the coating, required more interfacial energy to nucleate in the substrate. Thus, the lattice parameter difference between the Ni-Al coating and superalloy substrate might attribute to the anomalies in the CA-25 specimen. These results demonstrate the impact of the bond coating microstructures for a single crystal superalloy, boost the understanding of the role of interfacial energy in recrystallization, and provide more details for the guideline of bond coating design.

Declaration of Competing Interest

The authors declare that they have no known competing financial interests or personal relationships that could have appeared to influence the work reported in this paper

Acknowledgements

This work was financially supported by the National Natural Science Foundation of China (No. 51801008 and No. 11902014) and the Fundamental Research Funds for the Central Universities. We acknowledge the support from the National Science and Technology Major Project (2017-VI-0002-0072 and 2017-VI-0010-0081) High-Performance Computing Platform.

Supplementary materials

Supplementary material associated with this article can be found, in the online version, at doi:10.1016/j.scriptamat.2023.115297.

References

[1] A. Rahman, R. Jayaganthan, S. Prakash, V. Chawla, R. Chandra, J. Alloys Compd. 472 (1) (2009) 478–483.
[2] R. Wang, X. Gong, H. Peng, Y. Ma, H. Guo, Appl. Surf. Sci. 326 (2015) 124–130.
[3] C.T. Yu, H.J. Liu, A. Ullah, Z. Bao, S. Zhu, F.H. Wang, Corros. Sci. 159 (2019), 108115.
[4] H. Yao, Z. Bao, M. Shen, S. Zhu, F. Wang, Appl. Surf. Sci. 407 (2017) 485–494.
[5] O. Culha, E. Celik, N.F. Ak Azem, I. Birlik, M. Toparli, A. Turk, J. Mater. Process. Technol. 204 (1) (2008) 221–230.
[6] J. He, H. Peng, S. Gong, H. Guo, Corros. Sci. 120 (2017) 130–138.
[7] P. Kiruthika, S.K. Makineni, C. Srivastava, K. Chattopadhyay, A. Paul, Acta Mater. 105 (2016) 438–448.
[8] J. Sun, J. Liu, J. Li, C. Chen, X. Wang, Y. Zhou, X. Sun, Scr. Mater. 205 (2021), 114209.
[9] W.S. Walston, J.C. Schaeffer, W.H.J.S. Murphy, Superalloy (1996) 9–18.
[10] H.U. Hong, J.G. Yoon, B.G. Choi, I.S. Kim, C.Y. Jo, Scr. Mater. 69 (1) (2013) 33–36.
[11] X. Gong, H. Peng, Y. Ma, H. Guo, S. Gong, J. Alloys Compd. 672 (2016) 36–44.
[12] D.K. Das, K.S. Murphy, S. Ma, T.M. Pollock, Metal. Mater. Trans. A 39 (7) (2008) 1647–1657.
[13] Y. Wang, H. Guo, H. Peng, L.Q. Peng, S. Gong, Intermetallics 19 (2) (2011) 191–195.
[14] R. Burgel, P.D. Portella, J. Preuhs, Superalloys (2000) 229–238.
[15] X. Song, M. Rettenmayr, C. Müller, H.E. Exner, Metal. Mater. Trans. A 32 (9) (2001) 2199–2206.
[16] C. Zambaldi, F. Roters, D. Raabe, U. Glatzel, Mater. Sci. Eng. 454 (2007) 433–440. -455.
[17] B. Radhakrishnan, G.B. Sarma, T. Zacharia, Acta Mater. 46 (12) (1998) 4415–4433.
[18] A. Dasgupta, P. Sharma, K. Upadhyayula, Int. J. Damage Mech. 10 (2) (2001) 101–132.
[19] P. Sharma, Int. J. Solids Struct. 41 (22) (2004) 6317–6333.
[20] C.E. Murray, J. Appl. Phys. 123 (4) (2018), 045106.
[21] L. Wang, Y. Zhang, Z. Zeng, H. Zhou, J. He, P. Liu, M. Chen, J. Han, D.J. Srolovitz, J. Teng, Y. Guo, G. Yang, D. Kong, E. Ma, Y. Hu, B. Yin, X. Huang, Z. Zhang, T. Zhu, X. Han, Science 375 (6586) (2022) 1261–1265.
[22] S. Sun, D. Li, C. Yang, L. Fu, D. Kong, Y. Lu, Y. Guo, D. Liu, P. Guan, Z. Zhang, J. Chen, W. Ming, L. Wang, X. Han, Phys. Rev. Lett. 128 (1) (2022), 015701.
[23] J. Wen, J. Li, J. He, Y. Chen, X. Yan, Q. Guo, Q. Zhou, L. Wei, J. Sun, H. Guo, Appl. Surf. Sci. 588 (2022), 152937.
[24] S. Ryu, K. Kang, W. Cai, Proc. Natl. Acad. Sci. U.S.A. 108 (13) (2011) 5174–5178.
[25] S. Yin, G. Cheng, G. Richter, H. Gao, Y. Zhu, ACS Nano 13 (8) (2019) 9082–9090.
[26] X. Gao, W. Ouyang, O. Hod, M. Urbakh, Phys. Rev. B 103 (4) (2021), 045418.
[27] J. Sun, L. Wei, Q. Li, S. Gong, H. Guo, Rare Metals 40 (3) (2021) 693–700.
[28] S. Plimpton, J. Comput. Phys. 117 (1) (1995) 1–19.
[29] G.P. Purja Pun, Y. Mishin, Philos. Mag. 89 (34–36) (2009) 3245–3267.
[30] A.R. Khoei, G.T. Eshlaghi, S. Shahoveisi, Mater. Sci. Eng. 809 (2021), 140977.
[31] A. Stukowski, Modelling and Simulation in, Mater. Sci. Eng. 18 (1) (2009), 015012.
[32] B. Sundman, B. Jansson, J.-O. Andersson, Calphad 9 (2) (1985) 153–190.
[33] C.M.F. Rae, R.C. Reed, Acta Mater. 49 (19) (2001) 4113–4125.

[34] S.M. Schwarz, B.W. Kempshall, L.A. Giannuzzi, Acta Mater. 51 (10) (2003) 2765–2776.
[35] V. Rühle, H. Kusumaatmaja, D. Chakrabarti, D.J. Wales, J. Chem. Theory Comput. 9 (9) (2013) 4026–4034.
[36] T. Zhu, J. Li, A. Samanta, A. Leach, K. Gall, Phys. Rev. Lett. 100 (2) (2008), 025502.
[37] T.D. Swinburne, M.-C. Marinica, Phys. Rev. Lett. 120 (13) (2018), 135503.